


RESEARCH ARTICLE | FEBRUARY 21 2023

# Two-dimensional perovskite functionalized fiber-type heterostructured scintillators

E. G. Rogers ; M. D. Birowosuto; F. Maddalena; ... et. al



*Appl. Phys. Lett.* 122, 081901 (2023)

<https://doi.org/10.1063/5.0137890>



CrossMark

### Articles You May Be Interested In

Optical properties of single crystal  $\text{Bi}_4\text{Ge}_3\text{O}_{12}$  from the infrared to ultraviolet

*Journal of Applied Physics* (October 2014)

Compositing orbital angular momentum beams in  $\text{Bi}_4\text{Ge}_3\text{O}_{12}$  crystal for magnetic field sensing

*Appl. Phys. Lett.* (September 2017)

Refractive indices and electro-optic coefficients of the eulitites  $\text{Bi}_4\text{Ge}_3\text{O}_{12}$  and  $\text{Bi}_4\text{Si}_3\text{O}_{12}$

*Journal of Applied Physics* (November 2003)



A total solution for low-temperature characterization

[Learn more >](#)



# Two-dimensional perovskite functionalized fiber-type heterostructured scintillators

Cite as: Appl. Phys. Lett. **122**, 081901 (2023); doi: [10.1063/5.0137890](https://doi.org/10.1063/5.0137890)

Submitted: 6 December 2022 · Accepted: 2 February 2023 ·

Published Online: 21 February 2023



View Online



Export Citation



CrossMark

E. G. Rogers,<sup>1,a)</sup> M. D. Birowosuto,<sup>2</sup> F. Maddalena,<sup>3</sup> C. Dujardin,<sup>4</sup> F. Pagano,<sup>5,6</sup> N. Kratochwil,<sup>5</sup> E. Auffray,<sup>5</sup> P. Krause,<sup>1</sup> and C. Bizzari<sup>1</sup>

## AFFILIATIONS

<sup>1</sup>School of Aerospace, Transport Systems and Manufacturing, Cranfield University, Cranfield, MK43 0AL, United Kingdom

<sup>2</sup>Łukasiewicz Research Network—PORT Polish Center for Technology Development, Stabłowska 147, 54-066 Wrocław, Poland

<sup>3</sup>CINTRA UMI CNRS/NTU/THALES 3288, Research Techno Plaza, 50 Nanyang Drive, Border X Block, Level 6, Singapore 637553, Singapore

<sup>4</sup>Institut Lumière Matière, UMR5306 Université Lyon 1-CNRS, Université de Lyon, 69622 Villeurbanne Cedex, France

<sup>5</sup>CERN, Esplanade des Particules 1, 1211 Meyrin, Switzerland

<sup>6</sup>Dipartimento di Fisica, University of Milano-Bicocca, Milan, Italy

<sup>a)</sup>Author to whom correspondence should be addressed: [edith.g.rogers@cranfield.ac.uk](mailto:edith.g.rogers@cranfield.ac.uk)

## ABSTRACT

A fiber-type heterostructured scintillator based on bismuth germanate ( $\text{Bi}_4\text{Ge}_3\text{O}_{12}$ ) functionalized with the 2D-perovskite butylammonium lead bromide ( $(\text{BA})_2\text{PbBr}_4$ ) has been fabricated, and its scintillation performance analyzed toward its use for fast timing applications such as time-of-flight Positron Emission Tomography. The pixel shows energy sharing between the matrix and filler component, confirming that the two components are in synergy.

© 2023 Author(s). All article content, except where otherwise noted, is licensed under a Creative Commons Attribution (CC BY) license (<http://creativecommons.org/licenses/by/4.0/>). <https://doi.org/10.1063/5.0137890>

Heterostructured scintillators could offer a solution to the fundamental payoff between good gamma capture (stopping power) and scintillation performance (ultra-fast and high light yield emission). Applied to the development of advanced Time-of-Flight Positron Emission Tomography (ToF-PET) scintillators, this translates into a detector with a dense, heavy scintillator component (matrix) and a fast scintillator one (filler) working in synergy through the transfer of recoil electrons generated through gamma capture (energy sharing). While the concept is appealing, the choice of filler material is vital for ensuring good performance as there is a need to balance the creation of fast photons with the reduction in stopping power due to the lower density and effective atomic number ( $Z_{\text{eff}}$ ) of the filler relative to the host matrix.

The growth in new fast scintillators, e.g., nanoparticle- (see, e.g., Refs. 1 and 2) and metal-organic framework<sup>3–5</sup>-based scintillators, and 2D and 3D perovskites,<sup>6–8</sup> opens up options for the filler component. Several potential materials have been experimentally investigated as fillers for higher energy (e.g., ToF-PET) applications, including plastics,<sup>9–11</sup> nanocomposites,<sup>12–14</sup> and  $\text{BaF}_2$ .<sup>10</sup> So far, however, these materials present different drawbacks, e.g., low stopping power/density or deep UV emission. Single crystal metal-organic two dimensional (2D)

perovskites are a promising class of materials for fiber-type heterostructured scintillators as they offer fast decay times (0.6–17 ns), moderately good densities ( $\sim 2\text{--}3.5\text{ g/cm}^3$ ), an effective atomic number ( $Z_{\text{eff}}$ ) of  $\sim 60$ , and light yields up to 40 000 ph/MeV for  $(\text{BA})_2\text{PbBr}_4$ ,<sup>6,15</sup> while the coincidence timing resolution of a  $\sim 5 \times 5 \times 2$  mm Li doped  $(\text{PEA})_2\text{PbBr}_4$  sample was recently measured to be  $84 \pm 5$  ps.<sup>16</sup> Recent modeling and simulation work utilizing these data suggest that, depending on the pixel design, it is possible to have  $(\text{BA})_2\text{PbBr}_4$  loaded bismuth germanate ( $\text{Bi}_4\text{Ge}_3\text{O}_{12}$ , BGO) based fiber-type heterostructures with the potential to significantly out-perform LSO as fast scintillators with higher equivalent stopping power for 511 keV gamma photons.<sup>15</sup> The tunable nature of perovskites also opens up their use for other types of heterostructured scintillator, for instance, for multi-spectral x-ray imaging.<sup>8</sup>

In this paper, a proof-of-concept fiber-type heterostructure is assembled through the *in situ* solution growth of the 2D-perovskite  $(\text{BA})_2\text{PbBr}_4$  in a machined BGO matrix, and the scintillation performance analyzed toward ascertaining its suitability as a fiber-type heterostructure with good energy sharing for fast timing applications such as ToF-PET.

A  $3 \times 3 \times 1$  mm BGO matrix was prepared by precision drilling a  $5 \times 5$  array of  $400 \mu\text{m}$  diameter channels with  $200 \mu\text{m}$  nearest-to-nearest spacing using a KERN Evo micro-CNC center with micro-spotter (Kyocera) and C-UMD micro-drill (Union Tools) bits. The matrix was post-processed through polishing using SiC papers (1200 and 2500 grit) and alumina slurries (5 and  $1 \mu\text{m}$  diameter) (Metprep Ltd.). The matrices were then functionalized through the *in situ* solution growth of  $(\text{BA})_2\text{PbBr}_4$  within the machined channels using the method described by Maddalena *et al.*<sup>17</sup> from a 3M stoichiometric solution of butylammonium bromide ((BA)Br) and lead bromide ( $\text{PbBr}_2$ ) in dimethylsulfoxide (DMSO, anhydrous) (see the method and schematic in Fig. 1 of the supplementary material for further detail). The inset in Fig. 1 displays the scintillation microscopy image of the resulting pixel measured under 35 kV x-ray excitation with the sample sitting on the camera (Andor Zyla HF-FOP, pixel pitch =  $6.5 \mu\text{m}$ ), facing the x-ray beam. The two components can be clearly distinguished, with the filled channels appearing as brighter circles within the BGO matrix.

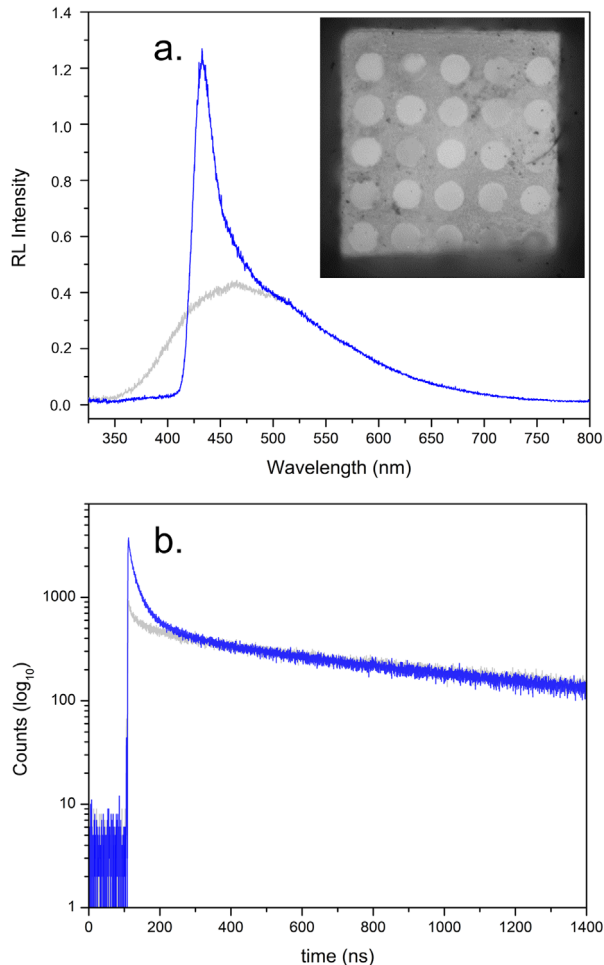


**FIG. 1.** (a) X-ray excited emission spectra and (b) x-ray excited decay time for a BGO monolith (grey line) and a BGO/ $(\text{BA})_2\text{PbBr}_4$  heterostructure (blue line). Inset: a scintillation microscopy image of the BGO/ $(\text{BA})_2\text{PbBr}_4$  pixel.

Radioluminescence spectra [Fig. 1(a)] for a bismuth germanate monolith (grey line) and the BGO/ $(\text{BA})_2\text{PbBr}_4$  heterostructure (blue line) were measured upon x-ray excitation by Bremsstrahlung x-rays from accelerated electrons (35 kV) bombarding a tungsten anode (Inel XRG 3000). The spectrum was measured using a SR500i-D2 monochromator (Andor) and an Andor Newton EM-CCD camera (DU970P-UVB) and was corrected for the spectral sensitivity of the system. Both spectra are dominated by the broadband BGO emission centered around 480 nm, while the spectrum measured for the heterostructure shows an additional narrow peak at around 435 nm ( $\sim 25\%$  of the total signal) due to  $(\text{BA})_2\text{PbBr}_4$ .<sup>6,18</sup> Additionally, the higher energy part of the BGO emission in the heterostructure below 425 nm ( $\sim 12\%$ ) is cut off, due to reabsorption by the perovskite. It is not possible from radioluminescence measurements to determine how much of the signal in the heterostructure is from the independent excitation of the components and how much is due to electron transfer from BGO to  $(\text{BA})_2\text{PbBr}_4$ , the intended mechanism in a heterostructured scintillator. Additionally, at 35 keV, the path length of a recoil electron, and therefore the probability of energy sharing, will be low. The perovskite nominally makes up 35% of the volume of the pixel and has an expected light output of 40 000 ph/MeV,<sup>6</sup> compared to 9000 ph/MeV for BGO. It would, therefore, be expected under 35 keV x-ray excitation that the signal from the perovskite would make up around 70.5% of the measured radioluminescence. The difference between the expected and measured intensity may be due to a lower than expected filling factor for  $(\text{BA})_2\text{PbBr}_4$  (voids in the channels). There is some evidence for this in the inset of Fig. 1, where some of the channels appear less bright than others. However, it is likely that there are also losses due to crystal quality issues (including crystallinity) that reduce the light output still further.

X-ray decay curves [Fig. 1(b)] were measured using pulsed x-rays with energies up to 30 keV generated at a 250 kHz repetition rate by a 405 nm picosecond diode laser (DeltaDiode from Horiba) focused on a x-ray tube (model N5084 from Hamamatsu). The resulting photons were collected by a PMA-C PMT from PicoQuant and histogrammed using time-correlated single-photon counting (PicoHarp300). The decay curve measured for the heterostructure shows additional fast decay components [ $\tau_1 = 3.20$  ns (21.88%),  $\tau_2 = 15.681$  ns (25.42%), and  $\tau_3 = 274.184$  ns (52.69%) at 450 nm] compared to BGO [ $\tau_1 = 2.934$  ns (0.68%),  $\tau_2 = 43.165$  ns (6.88%), and  $\tau_3 = 326.609$  ns (92.44%) at 500 nm] confirming the presence of the two materials. However, similar to the radioluminescence spectrum, while the impact of adding the perovskite on the timing response of the detector can clearly be seen, it is not possible to determine whether this additional signal results from the summation of the two components or from shared events where energy is transferred between the two components.

In order to clarify the mechanism of excitation, the 2D histograms of the integrated charge were measured using the setup described by Gundacker *et al.*<sup>19</sup> Samples were measured in coincidence with a reference crystal ( $2 \times 2 \times 3 \text{ mm}^3$  LSO:Ce:0.4%Ca, CTR =  $62 \pm 3$  ps FWHM) and a  $^{22}\text{Na}$  source. Splitting the signal independently optimized energy (analog amplifier) and time (high-frequency amplifier<sup>20</sup>) information. By measuring the integral and the amplitude of the energy signal, the different pulse shapes attributable to the two materials (from light yield and scintillation kinetics) were used to distinguish between events depositing energy in BGO, in perovskite, or in

both materials as described in Pagano *et al.*<sup>11</sup> [Figs. 2(a) and 2(b)]. The time integrated pulse height spectra for the BGO/(BA)<sub>2</sub>PbBr<sub>4</sub> heterostructure [Fig. 2(b)] contain three regions. The majority of events occur in the left-hand region where incoming photons only interact with BGO. The dominance of events in BGO to the overall response can be seen even more clearly in Fig. 2(c), where the data in Fig. 2(b) have undergone a coordinate transfer to pass from the [amplitude (V), integrated signal (V × ns)] to the [energy in perovskite (keV), energy in BGO (keV)] coordinate system. Here, correspondingly, most of the events occur in the region on the left hand side of the graph, where there is less than 50 keV deposited in the perovskite. Most of the energy is deposited in the matrix as is to be expected given the short length of the pixel (few absorbed events) and the greater volume of BGO (~65% of the pixel). This corresponds with what was observed in the radioluminescence spectrum [Fig. 1(a)].

The second area of interest in the lower part of Fig. 2(b) corresponds to events that occur solely in the perovskite. Between the two regions attributed to the individual components, there are events that correspond with shared events. This demonstrates that the measured signal is not just the sum of two independent components, but that there is a synergistic relationship between the BGO matrix and the

(BA)<sub>2</sub>PbBr<sub>4</sub> filler. Similar behavior has been observed for first generation plate-type heterostructured scintillators.<sup>9–11</sup> Figure 3 shows a schematic representation of the expected scintillation mechanism for heterostructured scintillators. This is a statistical process where different mechanisms can happen: paths A and B show events where gamma capture and conversion take place solely in the matrix or the filler, respectively. Path C represents two events: for (i), energy sharing will happen, as recoil electrons from photoelectric events travel far enough in the correct direction to reach the filler component and transfer their energy. For (ii), energy sharing does not happen, as the recoil electron travels away from the filler component.

The effect of energy sharing on coincidence timing resolution (CTR) can be observed in Fig. 4, which shows the CTR measured with a 511 keV <sup>22</sup>Na source for events occurring solely in BGO (green curve), and those shared between the matrix and the perovskite with at least 50 keV deposited in (BA)<sub>2</sub>PbBr<sub>4</sub> (blue curve). “Fast” events in this pixel (as shown in Fig. 2) are both directly excited and excited through energy sharing; however, the targeted aim for heterostructured scintillators is to maximize the number of shared events (increased detector efficiency). With this in mind, we focused on quantifying the impact of shared events only on the CTR. The CTR

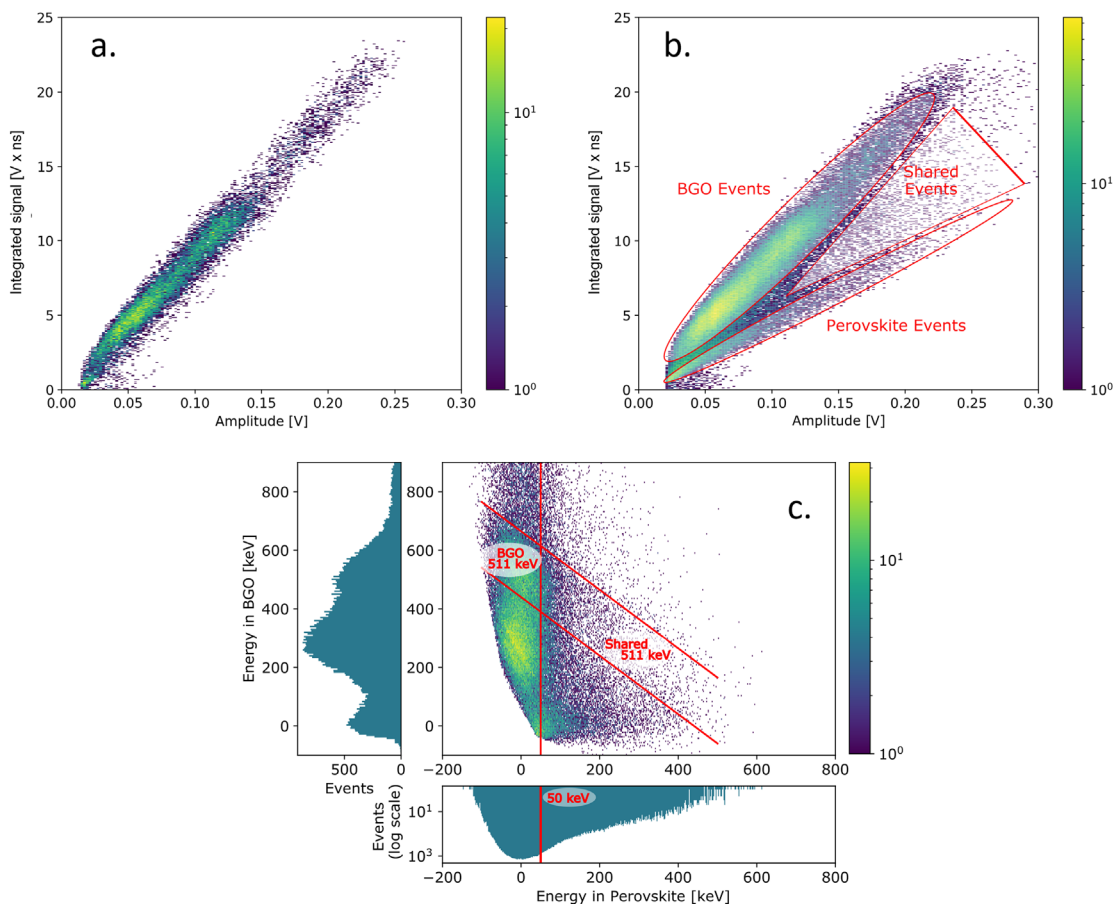


**FIG. 2.** Time integrated pulse height spectra for (a) BGO monolith and (b) a BGO/(BA)<sub>2</sub>PbBr<sub>4</sub> heterostructure. (c) Energy deposited in BGO (left axis) and perovskite (bottom axis).

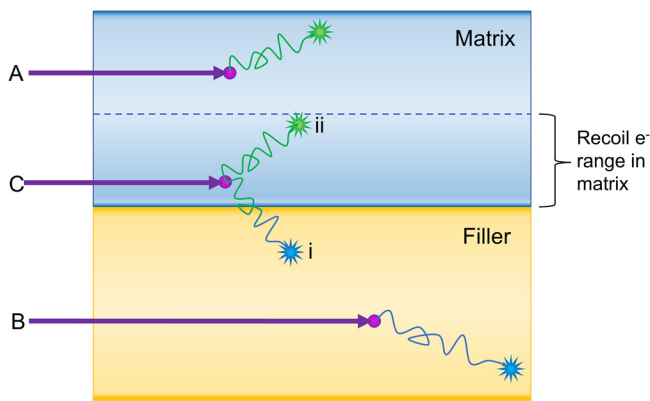


**FIG. 3.** Schematic diagram illustrating the proposed scintillation mechanism in a heterostructured scintillator. (a) An event where gamma conversion takes place solely in the matrix; (b) an event where gamma conversion takes place solely in the filler; and (c) (i) an event where the gamma photon is absorbed in the matrix, but recoil electrons are transferred to the filler (energy sharing), and (ii) an event where the recoil electron travels away from the filler (no energy sharing).

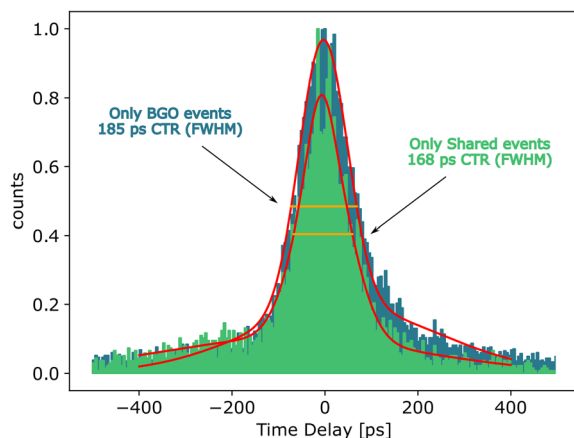


**FIG. 4.** Coincidence timing resolution of events in BGO only (blue) and events where at least 50 keV was deposited inside  $(\text{BA})_2\text{PbBr}_4$  (green). Red lines = Gaussian fit.

was obtained by evaluating the FWHM of the coincidence peak (obtained as the time delay between the high-frequency signals of the reference crystal and the sample) and by correcting it for the CTR of the reference crystal [ $CTR_{\text{sample}} = \sqrt{(2 \times FWHM^2 - CTR_{\text{ref}}^2)}$ ]. A decrease in the full width half maximum of the CTR from  $185 \pm 6$  to  $168 \pm 5$  ps can be seen. As the amount of energy sharing for this pixel, as illustrated in Fig. 2, is low, this, in turn, limits the reduction in CTR ( $CTR \propto \frac{1}{\sqrt{N}}$  where  $N$  = number of photons generated).

The ultimate aim for heterostructured detectors is to improve ToF-PET performance, which involves not only timing improvement but also maintaining a high stopping power (i.e., the accepted figure of merit for ToF-PET monolithic detectors performance is stopping power squared divided by CTR). Most of the current designs are focused primarily on improving timing (particularly plastic scintillator

functionalized plate-type designs) at the cost of maintaining a good stopping power. Moving to a fiber-type design with a higher  $Z_{\text{eff}}$  perovskite filler reduces the degradation in the stopping power from the loss of BGO. Furthermore, the direct comparison of the performance (timing, stopping power, and PET performance) of heterostructured scintillators is not a simple task as the designs, geometry, and filler/matrix materials impact the light transport and, in turn, the timing of the overall detectors. The method of measurement is also a problem, as the selection of different subpopulations of events can bias the timing and overestimate the real impact of the heterostructure approach. For now, only very general comparisons may be made. The 1 mm thickness of this pixel impacts its performance both through favoring timing and through both the reduction in fully absorbed events and ruling out quantitative comparisons of performance with the plate-type pixels studied by Turtos *et al.*<sup>9</sup> ( $3 \times 3 \times 3$  mm), Pagano *et al.*<sup>11</sup> ( $3 \times 3 \times 3$  and  $3 \times 3 \times 15$  mm), and Lecoq *et al.*<sup>10</sup> ( $3 \times 3 \times 15$  mm). However, in all cases, including this one, we can say that there is a reduction in CTR that can be linked to the presence of shared events, characteristic to the heterostructured scintillator concept.

The light yield of a heterostructured pixel such as the BGO/ $(\text{BA})_2\text{PbBr}_4$  pixel studied becomes dependent on the partition of energy between matrix only (9000 ph/MeV for BGO), filler only [40000 ph/MeV for  $(\text{BA})_2\text{PbBr}_4$ ], and shared events (varies statistically with values somewhere between those for the individual components depending on the degree of energy partition). Currently, fully absorbed events are still dominated by BGO absorption, so that the light output is biased toward that of BGO.

While the preliminary data for this pixel show that there is synergy between BGO and the perovskite, it can also be seen that the amount of energy sharing between the two components needs to be drastically increased before BGO/ $(\text{BA})_2\text{PbBr}_4$  fiber-type heterostructures can be used for fast timing applications such as ToF-PET. Maximization of both the number of fully absorbed and shared events and the resulting reduction in CTR is determined by the pixel design as well as the scintillation properties of the two components, with channel diameter and pitch, and pixel length heavily influencing performance.<sup>15</sup> Figure 5 shows the results of GEANT 4<sup>21</sup> simulations, modeling the effect of length on the performance of fiber-type heterostructures with this design using the methods from Krause *et al.*<sup>15</sup> It can be seen that both the equivalent stopping power (ESP) and the energy sharing (ES) scale with pixel length with energy sharing maximized for pixels longer than 15 mm.

To achieve real timing improvements while largely maintaining stopping power for 511 keV gamma photons, full length (15 mm +) pixels will be needed, and these are currently under development. From Fig. 5, it can be seen that by going from 1 to 15 mm length, the number of fully absorbed events in the pixel will increase from almost zero to around 23%. While this is lower than the 31% of fully absorbed events in an equivalent monolithic LSO pixel, it is significantly higher than that achieved by an equivalent BGO/plastic scintillator pixel. The significant increase in the energy sharing emulated in Fig. 5 from moving from 1 to 15 mm thickness (<1 to 33%) will, in turn, lead to significant improvements in the CTR. By further optimizing the layout of channels using a physics based approach to pixel design<sup>15</sup> (e.g., reduction of channel diameter and pitch), it will be possible to further improve heterostructure performance, and work is ongoing to develop

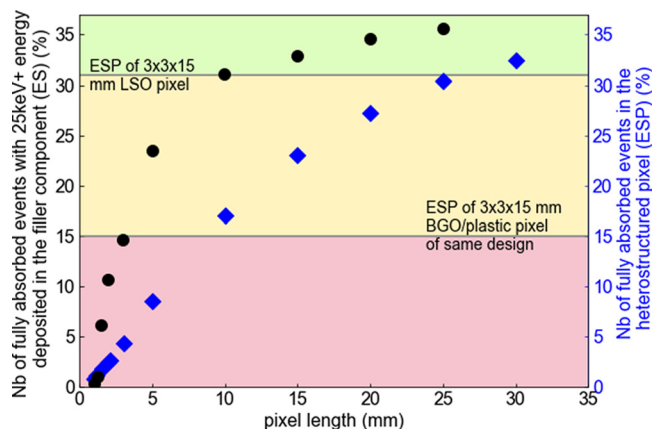


**FIG. 5.** GEANT4 simulation results showing the effect of length on the energy sharing (ES) capability [black circles (●), left axis] and the equivalent stopping power (ESP) [blue diamonds (◆), right axis] of a BGO/(BA)<sub>2</sub>PbBr<sub>4</sub> fiber-type heterostructure with a 5 × 5 array of 400 μm channels with 200 μm nearest-to nearest spacing. The graph is shaded to indicate areas where the pixel ESP represents (red) less than a 3 × 3 × 15 mm BGO/plastic scintillator of the same design, (yellow) greater than a 15 mm BGO/plastic scintillator of the same design, and (green) greater than the ESP of a 3 × 3 × 15 mm long monolithic LSO pixel. Shared events are ones where at least 25 keV is deposited in the filler.

a functionalized fiber-type pixel with a more optimized design. The flexibility in heterostructured scintillator construction opens up possibilities for further improving performance through changing the filler perovskite. Krause *et al.* also simulated the performance of heterostructures based around two other 2D perovskites: 2-(2-aminoethyl)isothioure lead bromide ((AEIU)PbBr<sub>4</sub>) and phenethyl ammonium lead bromide ((PEA)<sub>2</sub>PbBr<sub>4</sub>) and found that all three materials led to similar performance.<sup>15</sup> However, of these three, (BA)<sub>2</sub>PbBr<sub>4</sub> had the highest light yield by far. However, the rapid growth in the field of 2D-perovskites brings with it the potential for future materials with greater density (e.g., improved stopping power and energy sharing) and faster decay times (improved timing and CTR).

In this investigation, we establish that it is possible to functionalize a BGO fiber-type heterostructured scintillator with a fast-emitting 2D metal-organic perovskite ((BA)<sub>2</sub>PbBr<sub>4</sub>) through *in situ* solution growth and observe energy sharing between the two heterostructure components that leads to a reduction in the coincidence timing resolution of the pixel. While the prototype does not use an optimized layout, these results show that (BA)<sub>2</sub>PbBr<sub>4</sub> functionalized BGO fiber-type heterostructures show potential for fast timing applications such as time-of-flight positron emission tomography.

See the [supplementary material](#) for an overview of the synthesis route.

This work was supported by the UK Engineering and Physical Sciences Research Council (EPSRC) under Grant No. EP/S013652/1 for Cranfield University. This work was carried out in the framework of the Crystal Clear Collaboration and supported by the CERN budget for Knowledge Transfer to Medical applications and from the European Union's Horizon 2020 Research and Innovation programme under Grant Agreement No. 101004761 (N.K.). The authors acknowledge

financial support from the Ministry of Education (Singapore), under its AcRF Tier 2 Grant (No. MOE-T2EP50121-0012), the MERLION Program.

## AUTHOR DECLARATIONS

### Conflict of Interest

The authors have no conflicts to disclose.

## Author Contributions

**Edith Grace Rogers:** Formal analysis (equal); Investigation (equal); Resources (equal); Visualization (equal); Writing – original draft (lead); Writing – review & editing (lead). **M. Danang Birowosuto:** Investigation (equal); Methodology (equal); Resources (equal); Writing – review & editing (equal). **Francesco Maddalena:** Investigation (equal); Methodology (equal); Resources (equal); Writing – review & editing (equal). **Christophe Dujardin:** Formal analysis (equal); Investigation (equal); Methodology (equal); Visualization (equal); Writing – review & editing (equal). **Fiammetta Pagano:** Formal analysis (equal); Investigation (equal); Methodology (equal); Software (equal); Visualization (equal); Writing – review & editing (equal). **Nicolaus Kratochwil:** Formal analysis (equal); Investigation (equal); Methodology (equal); Software (equal); Visualization (equal); Writing – review & editing (equal). **Etiennette Auffray:** Formal analysis (equal); Funding acquisition (equal); Supervision (equal); Writing – review & editing (equal). **Philip Krause:** Software (equal); Writing – review & editing (equal). **Gregory Bizarri:** Conceptualization (lead); Formal analysis (equal); Funding acquisition (lead); Investigation (equal); Methodology (equal); Project administration (lead); Software (lead); Supervision (lead); Visualization (equal); Writing – review & editing (equal).

## DATA AVAILABILITY

The data that support the findings of this study are openly available in the Cranfield University at <http://doi.org/10.17862/cranfield.rd.21640520>, Ref. 22.

## REFERENCES

1. Liu, Z. Li, T. J. Hajagos, D. Kishpaugh, D. Y. Chen, and Q. Pei, “Transparent ultra-high-loading quantum dot/polymer nanocomposite monolith for gamma scintillation,” *ACS Nano* **11**, 6422–6430 (2017).
2. V. Shevelev, A. Ishchenko, A. Vanetsev, V. Nagirnyi, and S. Omelkov, “Ultrafast hybrid nanocomposite scintillators: A review,” *J. Lumin.* **242**, 118534 (2022).
3. J. Perego, I. Villa, A. Pedrini, E. C. Padovani, R. Crapanzano, A. Vedda, C. Dujardin, C. X. Bezuidenhout, S. Bracco, P. E. Sozzani, A. Comotti, L. Gironi, M. Beretta, M. Salomoni, N. Kratochwil, S. Gundacker, E. Auffray, F. Meinardi, and A. Monguzzi, “Composite fast scintillators based on high-Z fluorescent metal-organic framework nanocrystals,” *Nat. Photonics* **15**, 393 (2021).
4. J. Perego, C. X. Bezuidenhout, I. Villa, F. Cova, R. Crapanzano, I. Frank, F. Pagano, N. Kratochwil, E. Auffray, S. Bracco, A. Vedda, C. Dujardin, P. E. Sozzani, F. Meinardi, A. Comotti, and A. Monguzzi, “Highly luminescent scintillating hetero-ligand MOF nanocrystals with engineered Stokes shift for photonic applications,” *Nat. Commun.* **13**, 3504 (2022).
5. J.-X. Wang, L. Gutiérrez-Arzaluz, X. Wang, M. Almalki, J. Yin, J. Czaban-Jóźwiak, O. Shekhah, Y. Zhang, O. M. Bakr, M. Eddaoudi, and O. F. Mohammed, “Nearly 100 energy transfer at the interface of metal-organic frameworks for x-ray imaging scintillators,” *Matter* **5**, 253–265 (2022).

- <sup>6</sup>A. Xie, F. Maddalena, M. E. Witkowski, M. Makowski, B. Mahler, W. Drozdowski, S. V. Springham, P. Coquet, C. Dujardin, M. D. Birowosuto, and C. Dang, "Library of two-dimensional hybrid lead halide perovskite scintillator crystals," *Chem. Mater.* **32**, 8530–8539 (2020).
- <sup>7</sup>O. D. I. Moseley, T. A. S. Doherty, R. Parmee, M. Anaya, and S. D. Stranks, "Halide perovskites scintillators: unique promise and current limitations," *J. Mater. Chem. C* **9**, 11588–11604 (2021).
- <sup>8</sup>P. Ran, L. Yang, T. Jiang, X. Xu, J. Hui, Y. Su, C. Kuang, X. Liu, and Y. M. Yang, "Multispectral large-panel x-ray imaging enabled by stacked metal halide scintillators," *Adv. Mater.* **34**, 2205458 (2022).
- <sup>9</sup>R. M. Turtos, S. Gundacker, E. Auffray, and P. Lecoq, "Towards a metamaterial approach for fast timing in PET: experimental proof-of-concept," *Phys. Med. Biol.* **64**, 185018 (2019).
- <sup>10</sup>P. Lecoq, G. Konstantinou, R. Latella, L. Moliner, J. Nuyts, L. Zhang, J. Barrio, J. M. Benlloch, and A. J. Gonzalez, "Metascintillators: New results for TOFPET applications," *IEEE Trans. Radiat. Plasma Med. Sci.* **6**, 510 (2022).
- <sup>11</sup>F. Pagano, N. Kratochwil, M. Salomoni, M. Pizzichemi, M. Paganoni, and E. Auffray, "Advances in heterostructured scintillators: toward a new generation of detectors for TOF-PET," *Phys. Med. Biol.* **67**, 135010 (2022).
- <sup>12</sup>R. M. Turtos, S. Gundacker, S. Omelkov, B. Mahler, A. H. Khan, J. Saaring, Z. Meng, A. Vasil'ev, C. Dujardin, M. Kirm, I. Moreels, E. Auffray, and P. Lecoq, "On the use of CdSe scintillating nanoplatelets as time taggers for high-energy gamma detection," *npj 2D Mater. Appl.* **3**, 37 (2019).
- <sup>13</sup>K. Tomanová, A. Suchá, E. Mihóková, L. Procházková, I. Jakubec, R. M. Turtos, S. Gundacker, E. Auffray, and V. Čuba, "CsPbBr<sub>3</sub> thin films on LYSO:Ce substrates," *IEEE Trans. Nucl. Sci.* **67**, 933–938 (2020).
- <sup>14</sup>V. Vaněček, K. Děcká, E. Mihóková, V. Čuba, R. Král, and M. Nikl, "Advanced halide scintillators: From the bulk to nano," *Adv. Photonics Res.* **3**, 2200011 (2022).
- <sup>15</sup>P. Krause, E. Rogers, M. D. Birowosuto, Q. Pei, E. Auffray, A. N. Vasil'ev, and G. Bizzari, "Design rules for time of flight Positron Emission Tomography (ToF-PET) heterostructure radiation detectors," *Heliyon* **8**, e09754 (2022).
- <sup>16</sup>R. Cala, I. Frank, F. Pagano, F. Maddalena, C. Dang, M. D. Birowosuto, and E. Auffray, "Sub-100-picosecond time resolution from undoped and li-doped two-dimensional perovskite scintillators," *Appl. Phys. Lett.* **120**, 241901 (2022).
- <sup>17</sup>F. Maddalena, A. Xie, Arramel, M. E. Witkowski, M. Makowski, B. Mahler, W. Drozdowski, T. Mariyappan, S. V. Springham, P. Coquet, C. Dujardin, M. D. Birowosuto, and C. Dang, "Effect of commensurate lithium doping on the scintillation of two-dimensional perovskite crystals," *J. Mater. Chem. C* **9**, 2504–2512 (2021).
- <sup>18</sup>Y. Li, L. Chen, B. Liu, P. Jin, R. Gao, L. Zhou, P. Wan, Q. Xu, and X. Ouyang, "Scintillation performance of two-dimensional perovskite (BA)<sub>2</sub>PbBr<sub>4</sub> microcrystals," *J. Mater. Chem. C* **9**, 17124–17128 (2021).
- <sup>19</sup>S. Gundacker, R. M. Turtos, E. Auffray, M. Paganoni, and P. Lecoq, "High-frequency SiPM readout advances measured coincidence time resolution limits in TOF-PET," *Phys. Med. Biol.* **64**, 055012 (2019).
- <sup>20</sup>J. W. Cates, S. Gundacker, E. Auffray, P. Lecoq, and C. S. Levin, "Improved single photon time resolution for analog SiPMs with front end readout that reduces influence of electronic noise," *Phys. Med. Biol.* **63**, 185022 (2018).
- <sup>21</sup>S. Agostinelli, J. Allison, K. Amako, J. Apostolakis, H. Araujo, P. Arce, M. Asai, D. Axen, S. Banerjee, G. Barend, F. Behner, L. Bellagamba, J. Boudreau, L. Broglia, A. Brunengo, H. Burkhardt, S. Chauvie, J. Chuma, R. Chytráček, G. Cooperman, G. Cosmo, P. Degtyarenko, A. Dell'Acqua, G. Depaola, D. Dietrich, R. Enami, A. Feliciello, C. Ferguson, H. Fesefeldt, G. Folger, F. Foppiano, A. Forti, S. Garelli, S. Giani, R. Giannitrapani, D. Gibin, J. Gómez Cadenas, I. González, G. Gracia Abril, G. Greeniaus, W. Greiner, V. Grichine, A. Grossheim, S. Guatelli, P. Gumplinger, R. Hamatsu, K. Hashimoto, H. Hasui, A. Heikkinen, A. Howard, V. Ivanchenko, A. Johnson, F. Jones, J. Kallenbach, N. Kanaya, M. Kawabata, Y. Kawabata, M. Kawaguti, S. Kelner, P. Kent, A. Kimura, T. Kodama, R. Kokoulin, M. Kossov, H. Kurashige, E. Lamanna, T. Lampén, V. Lara, V. Lefebvre, F. Lei, M. Liendl, W. Lockman, F. Longo, S. Magni, M. Maire, E. Medernach, K. Minamimoto, P. Mora de Freitas, Y. Morita, K. Murakami, M. Nagamatu, R. Nartallo, P. Nieminen, T. Nishimura, K. Ohtsubo, M. Okamura, S. O'Neale, Y. Oohata, K. Paech, J. Perl, A. Pfeiffer, M. Pia, F. Ranjard, A. Rybin, S. Sadilov, E. Di Salvo, G. Santin, T. Sasaki, N. Savvas, Y. Sawada, S. Scherer, S. Sei, V. Sirotenko, D. Smith, N. Starkov, H. Stoecker, J. Sulkimo, M. Takahata, S. Tanaka, E. Tcherniaev, E. Safai Tehrani, M. Tropeano, P. Truscott, H. Uno, L. Urban, P. Urban, M. Verderi, A. Walkden, W. Wander, H. Weber, J. Wellisch, T. Wenaus, D. Williams, D. Wright, T. Yamada, H. Yoshida, and D. Zschiesche, "GEANT4—A simulation toolkit," *Nucl. Instrum. Methods Phys. Res., Sect. A* **506**, 250–303 (2003).
- <sup>22</sup>See <http://doi.org/10.17862/cranfield.rd.21640520> for "Cranfield University."